Macromolecules **2006,** *39,* 439−447

Temperature-Dependent Thermal and Elastic Properties of the Interlamellar Phase of Semicrystalline Polyethylene by Molecular Simulation

Pieter J. in 't Veld,[†] Markus Hütter,[‡] and Gregory C. Rutledge*

Department of Chemical Engineering, Massachusetts Institute of Technology,
Cambridge, Massachusetts 02139

Received August 29, 2005; Revised Manuscript Received October 18, 2005

ABSTRACT: We present the first theoretical estimates for thermoelastic properties of the noncrystalline domain (the "interlamellar phase") of semicrystalline polyethylene obtained by Monte Carlo simulations. The interlamellar phase is prescribed to be thermodynamically metastable, with the constraints that it have an average density less than that of the crystal and that it be bounded by two static crystalline lamellae oriented with the {201} crystal plane parallel to the interface. Polyethylene was modeled using a realistic united atom force field with inclusion of torsional contributions, and the results are compared to those of prior studies that used a freely rotating chain model. Parallel tempering between 350 and 450 K was used to simulate several isochoric/isothermal ensembles simultaneously and efficiently, from which the heat capacity, thermal expansion coefficients, Grüneisen coefficients, and the elastic stiffness tensor were determined at atmospheric pressure. The noncrystalline interlamellar phase exhibits properties intermediate between that of the semicrystalline solid and the amorphous melt.

Introduction

In semicrystalline polymers, one of the unique features of morphology is the noncrystalline, interlamellar material. Over the years, the nature of this material has been the subject of much debate, in no small part due to inferences that were drawn about the structure of this material based on the prevailing theories of polymer crystallization. The structure of the noncrystalline material, however, has generally eluded direct experimental characterization because it arises as an intermediate domain between crystallites in a heterogeneous, semicrystalline material. Efforts to characterize this domain in the presence of coexisting crystal and amorphous phases is complicated by the presence and overlap of signals from several different phases and uncertainty in the assignment of a particular response, e.g., spectral signature, to the interlamellar domain material.[1,2] Attempts to isolate physically the interlamellar domain or its interface with the crystal lamellae, for example by selective degradation, are subject to reconstruction of the remaining material as constraints on the interlamellar phase are released.[3] Last, in crystalline polymers such as polyethylene where crystal phase relaxations are present, causal relationships between the kinetics of crystal formation and the structure of the interlamellar material are subject to fading memory.[4]

In addition to questions of a physicochemical nature regarding the structure of the interlamellar material, there is also a need to characterize better the properties of this material. In two-phase composite models, it is usually assumed that the properties of the interlamellar material are comparable to those of the unconstrained amorphous melt, or else in the other extreme it may be assumed that the properties of the interlamellar material are inextricably combined with those of the crystal.[5−7] In three-phase composite models, the properties of the interlamellar domain are considered to exhibit both unconstrained and constrained amorphous character, with the amount of the latter being treated generally as an adjustable parameter.[8,9] Crist et al. reported that the elastic properties of the interlamellar phase varies with crystallinity, which they attributed to the role of lamellar thickness in suppressing the crystalline α_c-relaxation.[10] To test such models and to eliminate ambiguity, it is desirable to have independent confirmation of the properties of the interlamellar, noncrystalline material, by which it would be possible to place bounds on the resulting properties of the heterogeneous semicrystalline, composite-like material.

To address some of these issues, we have previously reported a molecular level simulation that has been shown to capture the essential features of the interlamellar domain.[11−13] The simulation is predicated on the existence of a thermodynamically rigorous definition of metastability that prevents the molecular model from collapsing into a single homogeneous phase of either melt or crystalline order. This is accomplished through the introduction of constraints on the simulation that are inconsistent with either a single phase melt or crystal.[14,15] In the current implementation, this is accomplished through imposition of crystalline boundaries on a simulation performed at melt-like densities. This simple model has been shown to produce a realistic picture of the variation in site density and local chain orientation across the interface between crystalline and amorphous zones of the interlamellar domain,[11,12] and to reveal significant differences in the structure of the interface when the chains in the crystal are tilted with respect to the lamellar normal, as in the {201} interface.[13] However, all these prior works were performed using a freely rotating chain model (FRC) that resembles polyethylene in its chemical structure and interatomic packing interactions, but was made artificially more flexible in order to expedite the molecular simulation. More recently, we reported the first results of the method applied to a fully realistic model of polyethylene (PE), complete with 3-fold torsional potential.[16] There, the focus was on the crystal/amorphous interface. Here, we treat the entire interlamellar phase of PE as a representative volume element and compute its thermodynamic

---

* Corresponding author: rutledge@mit.edu.

[†] Current address: Sandia National Laboratories, MS 1415, Albuquerque, NM 87185.

[‡] Current address: Department of Materials, Institute for Polymers, Swiss Federal Institute of Technology (ETH), CH-8093 Zürich, Switzerland.

10.1021/ma0518961 CCC: $33.50

properties over a range of temperatures. We also compare these with what we observed previously for the freely rotating chain model.[17]

Methodology

Force Field. In the current paper, we use the united atom model for polyethylene, including the torsion angle terms, described originally by Paul et al.[18] and modified subsequently by Bolton et al.[19] and by In ’t Veld and Rutledge.[17] This force field has previously been shown to describe accurately both the structure and dynamics of the amorphous PE melt, crystallization and melting transitions for *n*-alkanes and PE, and structure and kinetics of lamellar crystallization of PE from the melt.[18−21] The stable crystal phase, though similar to that for PE, is actually pseudohexagonal. A Lennard-Jones potential is used to compute the nonbonded CH_2 interactions between all united atom pairs on different chain segments and those separated by four or more bonds in the same chain segment

$$E_{\mathrm{LJ},ij} = 4\epsilon_{\mathrm{LJ}}\left[\left(\frac{\sigma_{\mathrm{LJ}}}{d_{ij}}\right)^{12} - \left(\frac{\sigma_{\mathrm{LJ}}}{d_{ij}}\right)^{6}\right], \quad d_{ij} = |\Delta\mathbf{r}_{ij}|, \Delta\mathbf{r}_{ij} = \mathbf{r}_i - \mathbf{r}_j \tag{1}$$

where $\epsilon_{\mathrm{LJ}} = 390.95$ J/mol and $\sigma_{\mathrm{LJ}} = 0.4009$ nm; $\mathbf{r}_i$ and $\mathbf{r}_j$ represent the Cartesian coordinates of sites *i* and *j*. Nonbonded interactions are truncated at a cutoff distance $r_c = 2.5\sigma_{\mathrm{LJ}}$ and corrected for long-range contributions. The bond stretching potential is harmonic in bond length

$$E_{l,i} = \frac{1}{2}k_l(l_i - l_0)^2 \tag{2}$$

where l_i is the length of bond *i*; the bond stretching constants are $k_l = 376.1 \times 10^6$ J/mol/nm^2 and $l_0 = 0.1530$ nm. The bond angle bending potential is harmonic in the cosine of the bond angle complement

$$E_{\theta,i} = \frac{1}{2}\frac{k_\theta}{\sin^2\theta_0}(\cos\theta_i - \cos\theta_0)^2 \tag{3}$$

where θ_i is the complement of the bond angle constructed by bond *i* and *i*-1; the angle bending constants are $k_\theta = 502.1$ kJ/mol and $\theta_0 = 68.0°$. After rearrangement using trigonometric identities, the bond torsion potential has the form

$$E_{\phi,i} = \sum_{n=0}^{3} k_n \cos^n\phi_i \tag{4}$$

where ϕ_i is the bond torsion angle constructed by bond pairs $\{i, i-1\}$ and $\{i-1, i-2\}$; the torsion constants are $k_n \in \{6.498, -16.99, 3.626, 27.11\}$ kJ/mol. Here, $\cos\phi_i$ is calculated using

$$\Delta\mathbf{r}_i = \mathbf{r}_i - \mathbf{r}_{i-1}, \quad \mathbf{n}_i = \Delta\mathbf{r}_i \times \Delta\mathbf{r}_{i-1}, \quad \cos\phi_i = \frac{\mathbf{n}_i\cdot\mathbf{n}_{i-1}}{|\mathbf{n}_i||\mathbf{n}_{i-1}|} \tag{5}$$

where $\mathbf{r}_i$ represents the position vector of united atom site *i* and $\Delta\mathbf{r}_i$ is the bond vector between two bonded sites. Note that in this convention the torsion angle assumes a value of 180 degrees in the trans state, which differs from the convention employed by Bolton et al.[19] The total torsion potential is obtained by summing over all available torsion angles.

Virial Calculation of Stress. We calculate the virial equation of stress as described by In ’t Veld and Rutledge,[17] with addition of the torsion contribution to the virial equation

$$\mathbf{W}_{\phi,i} = [\Delta\mathbf{r}_{i-2}^t(\Delta\mathbf{r}_{i-1} \times \mathbf{g}_{-1}) + \Delta\mathbf{r}_{i-1}^t(\Delta\mathbf{r}_i \times \mathbf{g}_0 - \Delta\mathbf{r}_{i-2} \times \mathbf{g}_{-1}) - \Delta\mathbf{r}_i^t(\Delta\mathbf{r}_{i-1} \times \mathbf{g}_0)] \sum_{n=1}^{3} n\, k_n \cos^{n-1}\phi_i \tag{6}$$

where

$$\mathbf{g}_{-1} = \frac{1}{l_{i-1}}\left(\frac{\mathbf{n}_i}{l_i} + \frac{\mathbf{n}_{i-1}}{l_{i-1}}\cos\phi_i\right), \quad \mathbf{g}_0 = \frac{1}{l_i}\left(\frac{\mathbf{n}_{i-1}}{l_{i-1}} + \frac{\mathbf{n}_i}{l_i}\cos\phi_i\right) \tag{7}$$

The total torsion contribution for an amorphous isotropic system of linear chains is normally zero.[22] However, in our particular case, chains are effectively tethered to an immobile crystal surface, which gives rise to nonzero contributions. With the addition of the torsion contribution, the total instantaneous stress tensor σ is given by

$$\sigma = -\frac{1}{\mathrm{V}}\left[\sum_{i=1}^{N_{sites}-1}\sum_{j=i+1}^{N_{sites}} \mathbf{W}_{\mathrm{LJ},ij} + \sum_{i=1}^{N_l}\mathbf{W}_{l,i} + \sum_{i=1}^{N_\theta}\mathbf{W}_{\theta,i} + \sum_{i=1}^{N_\phi}\mathbf{W}_{\phi,i} + \mathbf{W}_{ideal}\right] \tag{8}$$

which is the summation over all contributions due to Lennard-Jones interactions, bond lengths, bond angles, and bond torsions. Relations for the remaining terms in eq 8 are provided in ref 17.

Simulation Method. The simulation box consisted of an immobile crystal phase and a mobile interlamellar phase—the combination of both interfacial material and truly amorphous material—as a model for semicrystalline polyethylene. Because of the use of the united atom force field, we adjusted the polyethylene crystal unit cell from orthorhombic to pseudohexagonal symmetry in order to satisfy atmospheric pressure conditions at 400 K within the crystal phase. Specifically, the undeformed unit cell had $a = 0.77479$ nm, $b = 0.44626$ nm, and $c = 0.251822$ nm, with all crystallographic angles being 90°. To represent the crystal lamella, we constructed an array of 3 by 4 by 5 unit cells (2.32 nm × 1.79 nm × 1.26 nm, density 1.068 g/cm^3) oriented with the {201} plane normal to the *z*-direction of the simulation cell. The choice of a {201}-oriented crystal is supported by both experimental evidence[23] and previous simulation results,[13] which suggest a minimum in interfacial energy for this particular orientation. An initial configuration of the {201}-oriented crystal was constructed of 24 chain segments with 80 united atom CH_2 sites in an orthorhombic box. We immobilized the first and last five sites of each chain segment. 18 chain segments were then selected at random to serve initially as bridge molecules. The remaining six chain segments were split in half to form 12 tails, and a total of 384 sites were then deleted from the mobile ends of the tails to satisfy approximately the target interlamellar density of 0.7947 g/cm^3. The interlamellar density then was fine-tuned by deforming affinely the mobile region in the direction perpendicular to the crystal surface—hereafter referred to as the *z*-direction—to match the target density exactly. The resulting interlamellar phase model spanned 7.66 nm in the *z*-direction between two crystal lamellae and, at a density of 0.7947 g/cm^3, exhibited an internal thermodynamic stress, summed over the entire interlamellar phase, equal to atmospheric pressure at 402 K. The final configuration consisted of 30 chain segments (18 bridges and 12 tails), with a total of 1536 united atom sites, of which 1296 sites were mobile in the simulation. Figure 1 displays a schematic representation of the simulation cell. The

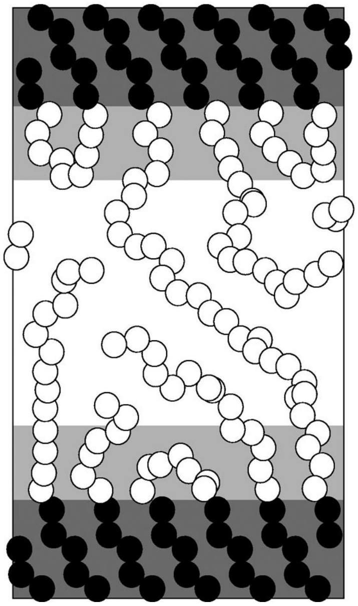

Figure 1. Schematic rendering of a simulation cell depicting an immobile crystalline phase (black beads on a darker background) and a mobile interlamellar phase (white beads). The lighter background denotes the subset of mobile beads forming the interphase, while the white background represents the beads forming the amorphous phase. The fraction of material that comprises the interphase is determined dynamically by the simulation.

five sites on each anchored end of the chain segments and immobilized within the crystal were sufficient to capture all contributions from the crystal phase to energy and stress in the interlamellar domain. The same simulation is representative of semicrystalline morphologies having thicker crystal lamellae. For example, if the crystal thickness is assumed to be 13.6 nm, then the simulation maps to a semicrystalline polyethylene having molecular weight of 10 100 g/mol and 64% crystallinity.[14] It is worth noting that the interlamellar spacing and crystallinity used here are typical of polyethylene and are within 15% of values cited by Hoffman for the canonical model of a semicrystalline polyethylene.[24] The interlamellar spacing is within 30% of that reported by Crist et al. for a wide range of crystallinity.[10]

Once created, randomization of the initial configuration was performed at $T = 10\,000$ K for 1000 cycles to ensure rapid amorphization of the interlamellar phase. Phase space was sampled in Metropolis Monte Carlo fashion through the use of topology-altering (end-reptation and end-bridging) and displacement moves (end-rotation, re-bridging, and single-site displacement), as explained previously.[17] Importantly, during simulation the end-bringing Monte Carlo move converts bridge-tail pairs to tail-loop pairs, and vice versa, thereby ensuring equilibrated distributions of loops and bridges at each temperature. This has been described at length in earlier reports.[10−13,16] In addition, we facilitated a more efficient sampling of phase space at lower temperatures by applying parallel tempering. Ten such randomized configurations were quenched to the desired temperature profile and equilibrated for 25 000 cycles before any measurements were taken. In contrast to our previous paper,[17] for efficiency purposes, we increased the frequency of parallel tempering moves to one per 1000 Monte Carlo moves. Our parallel tempering scheme used a temperature profile as prescribed by Kofke[25] to ensure equal swapping probability between neighboring temperatures; an acceptance of ~35% was observed at all temperatures. The temperature profile used here consisted of simulations at $T \in \{350, 359.9, 370.1, 380.6, 391.4, 402.4, 413.8, 425.6, 437.6, 450\}$ K. Decay studies of the energy and end-to-end autocorrelation function confirm equilibration in 25 000 cycles (one cycle equals 1536 Monte Carlo moves).

For purposes of elastic property calculations, united atom sites were displaced affinely with strain, either as entire rigid segments or as individual united atom sites for the crystal and interlamellar domains, respectively. Sites in the rigid crystal segments were displaced with respect to a common reference or anchor point, defined as the intersection of the segment's molecular axis with the nearest simulation box face in the z-direction (at $z = \pm{}^1/_2L_z$). Once deformed, a configuration was equilibrated for 25 000 cycles. With a few unimportant exceptions, tensile and compressive deformations were simulated at $\epsilon_i \in \{0.00\%, \pm1.25\%, \pm2.50\%, \pm3.75\%, \pm5.00\%, \pm6.25\%, \pm7.50\%, \pm8.75\%\}$ for $i = 1, 2, 3$. Combined tensile deformations, used in calculation of the off-diagonal stiffness coefficients, were simulated for values of pairs $\epsilon_i = \epsilon_j \in \{0.00\%, \pm0.63\%, \pm1.25\%, \pm1.88\%, \pm2.50\%, \pm3.13\%, \pm3.75\%, \pm4.38\%\}$ for i, $j = 1,2,3$; $i \neq j$. Shear deformations were performed under simple shear for $\epsilon_i \in \{0.00\%, \pm1.25\%, \pm2.50\%, \pm3.75\%, \pm5.00\%\}$ for $i = 4,5,6$. Altogether, 1130 points in phase space were simulated on 220 1.0 GHz Pentium III processors over a period of 1 month.

Thermal and Elastic Properties. The calculation of elastic properties was performed by canonical $N\mathbf{h}T$ simulation on a grid of points in (T, $\mathbf{h}$) space, where $\mathbf{h}$ is the tensor that describes both the size and shape of the system, e.g. $V = \det(\mathbf{h})$.[26] Lines of constant stress can be obtained through interpolation of the calculated virial stress at each grid point. Our motivation for using the isochoric/isothermal ensemble in this way is 2-fold. First, we can conveniently determine properties at either constant volume or constant pressure. Second, due to the fact that small changes in the volume normally correspond to large changes in the stress, it is more accurate and efficient to perform the simulations in the $N\mathbf{h}T$ ensemble than the $N\boldsymbol{\sigma}T$ ensemble.

The transformation of any property $X(V,T)$ to any property $X(P,T)$ forms the basis of our constant pressure calculations and is obtained by determining $P(V,T)$, thus creating the ability to construct $X(P(V,T), T)$. At each state point, pressure is calculated as

$$P(T,V) = -\frac{1}{3}\sum_{i=1}^{3}\sigma_i(T,\mathbf{h}) \tag{9}$$

where only the contributions to stress from the noncrystalline interlamellar phase are included. Continuity between the crystal lamellae and the interlamellar phase imposes constraints on two of the three cell vectors used to define $\mathbf{h}$, so there is a one-to-one relation between the cell dimension L_z perpendicular to the interface and the cell volume itself; it is sufficient to vary either L_z or V, equivalently, to change the interlamellar phase pressure, at each temperature. A least mean square fit of P to a second-order Taylor series expansion in L_z was used for this purpose to determine $P(V)$. In this work, the pressure of interest was $P_0 = 1$ atm. Thus, we determined $V_0(T)$, the cell volume at which $P = 1$ atm, by interpolating pressure as a function of volume at each temperature to identify the curve of constant $P = 1$ atm.

Isochoric and isobaric heat capacities at atmospheric pressure were obtained from the simulation data for $E(V,T)$. First, the data for $E(V,T)$ was fit by least mean squares to a second-order Taylor series expansion in T at each simulated value of V. From the resulting analytical expressions, $C_v = (\partial E/\partial T)|_V$ can be estimated at any value of T and, by interpolation, at any value of V, within the ranges simulated; in particular, $C_v(V_0(T))$ was used to construct the temperature dependence of the isochoric heat capacity at $P = 1$ atm. This is subtly different from the isobaric heat capacity, which requires the change in internal energy with temperature at constant pressure, as shown in eq 10,

$$C_p = \left(\frac{\partial H}{\partial T}\right)_P = \left(\frac{\partial E}{\partial T}\right)_P + P\left(\frac{\partial V}{\partial T}\right)_P \tag{10}$$

To compute the first term of eq 10 (at $P = 1$ atm), the data for $E(V,T)$ were fit by least mean squares to a second-order Taylor expansion in V at each value of T, from which the values for $E(V_0)$, corresponding to internal energy along the $P = 1$ atm isobar, were determined. These were then fit by least mean squares to a second-order Taylor expansion in T and, from the resulting analytical expression, $(\partial E/\partial T)|_P$ determined. To compute the second term of eq 10 (also at $P = 1$ atm), the data for $V_0(T)$ were also fit to a second-order Taylor expansion in T.

Stresses were calculated as functions of strain and temperature. For each temperature, each component of stress was fit to a second-order Taylor series expansion of the form

$$\sigma_i = \sigma_{0,i} + \sum_{j=1}^{6} \epsilon_j \left[\left(\frac{\partial \sigma_i}{\partial \epsilon_j}\right)_0 + \frac{1}{2}\sum_{k=1}^{6} \epsilon_k \left(\frac{\partial^2 \sigma_i}{\partial \epsilon_j \partial \epsilon_k}\right)_0\right] \tag{11}$$

where subscript 0 denotes expansion about the $P = 1$ atm reference volume $V_0(T)$ at each specific temperature. Note that, in contrast to our previous work,[17] where the reference volume was the same for all temperatures, here the reference volume itself is taken to be temperature dependent, in accordance with deformation occurring about the equilibrium, $P = 1$ atm simulation cell at each temperature. Furthermore, even though strains are imposed both perpendicular to and within the plane of the crystal surface, only contributions from the noncrystalline interlamellar phase are included in the calculated stress. With this construction, we computed the elastic moduli of the noncrystalline interlamellar phase using

$$C_{ij} = \left(\frac{\partial \sigma_i}{\partial \epsilon_j}\right)_{T,\epsilon_{k\neq j}} \tag{12}$$

The second-order derivative in eq 11 provides a measure of the nonlinearity of the stress response with respect to strain. At the extremes of strain (±8.75%), nonlinear terms ran as high as 65% of the linear, Hookean terms in some instances.

Grüneisen coefficients γ_i ($i = 1, 2, 3$) provide a measure of entropic contributions to the elastic moduli according to

$$\gamma_i = -\frac{V_0}{C_V}\left(\frac{\partial \sigma_i}{\partial T}\right)_{V=V_0} = \frac{1}{C_V}\left(\frac{\partial S}{\partial \epsilon_i}\right)_{T,\epsilon_{k\neq i}} \tag{13}$$

They were calculated at atmospheric pressure following a procedure similar to that used to compute the isochoric heat capacity, but with stress substituted for energy.

Results and Discussion

Conformational Properties. Figures 2 and 3 show density and order profiles, respectively, for an interlamellar phase flanked by {201}-oriented crystal phases. To enhance the statistics, we mirrored profiles of density and orientational order around the center plane of the simulation cell. The ordered layering of atoms characteristic of the crystal extend farther into the interlamellar domain with decreasing temperature, indicative of a thickening of the interface, or crystal/amorphous interphase.

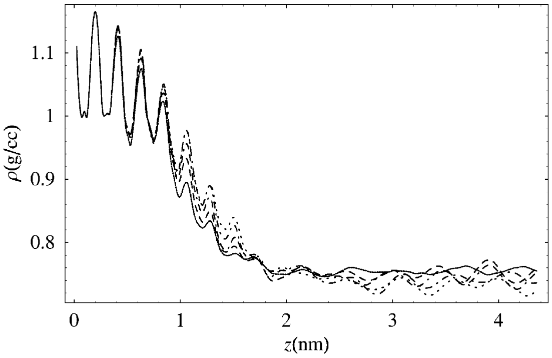

Figure 2. Density profiles of the undeformed state at T(K) ∈ {350, 370.1, 391.4, 413.8, 437.6} in order from dotted to solid curves.

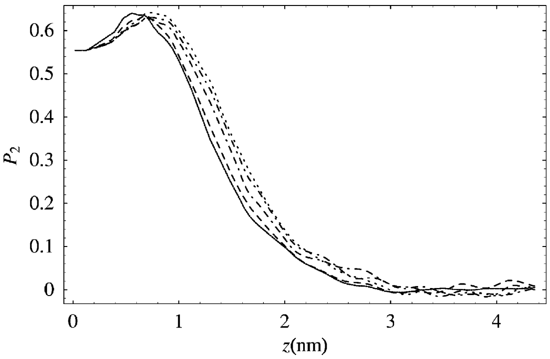

Figure 3. Absolute orientation profiles of the undeformed state at T(K) ∈ {350, 370.1, 391.4, 413.8, 437.6} in order from dotted to solid curves. P_2 is the bond orientation order parameter, $P_2 = {}^3/_2\langle\cos^2\phi\rangle - {}^1/_2$, where ϕ is the angle measured with respect to the z-direction of the vector joining the nearest neighbors of each atom.

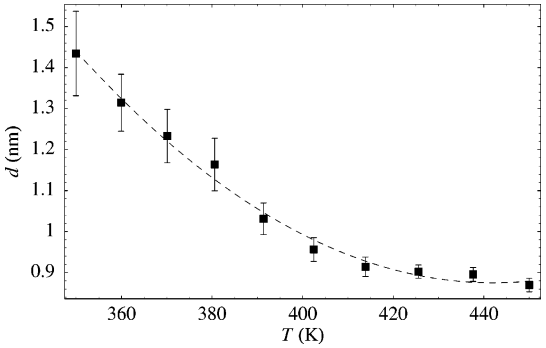

Figure 4. Interface thickness measured by the method of Gibbs dividing surfaces as a function of temperature in the undeformed state.

To quantify the interphase thickness, we invoke the concept of a Gibbs dividing surface, the plane that partitions the mass located in the finite width interphase equally to the adjoining amorphous and crystal phases, as described elsewhere.[16] The interphase thickness is then defined as twice the distance of the Gibbs dividing surface from the surface of the immobile crystal phase. The crystal surface is defined midway between the top layer of atoms in the crystal and the first layer of mobile atoms bonded to them. Figure 4 shows the interphase thickness as a function of temperature obtained from Gibbs dividing surfaces, as was done in ref 16. The data show a decrease in interphase thickness with increasing temperature, in accord with similar trends reported in ref 16 for PE and ref 17 for FRC: the higher the temperature, the weaker is the effect of the bond angle and torsion potential, and hence the shorter is the persistence length of the chain. In addition, entropic effects become more important, which altogether leads to a thinner interphase region at higher temperatures. (The small difference in interphase thickness between ref 16 and the current work is likely due to a difference in specification of pressure in the two works; ref 16 defines the amorphous region in the central portion (only) of the interlamellar phase to be at atmospheric pressure while in this work the pressure computed over the entire interlamellar phase is atmospheric.)

The average lengths of bridge, loop, and tail segments in the interlamellar phase as functions of temperature were investigated. As was the case for FRC,[13] in PE all three populations exhibit an exponential decay (not shown) in population $p(n_i)$ with increasing segment length, n_i, where n_i is the number of CH_2 groups in a segment of type i (bridge, loop or tail), and $p(n_i) \sim \exp(-\mu(n_i)/kT)$. This is due to the approximately linear dependence of chemical potential $\mu(n_i)$ on segment length. The average segment lengths for both bridge and tail populations were found to increase with increasing temperature, from $\langle n_{bridge}\rangle \approx 139$ and $\langle n_{tail}\rangle \approx 44$ at 350 K to $\langle n_{bridge}\rangle \approx 169$ and $\langle n_{tail}\rangle \approx 55$ at 450 K. The shift toward longer segments at higher temperature can be understood as a consequence of the $1/T$ dependence of $\mu(n_i)/kT$. All else being equal, this should also hold true for the loop population, since the chemical potential of loops and bridges of equal length would be comparable. Remarkably, the average length of loop segments decreases slightly with increasing temperature, from $\langle n_{loop}\rangle \approx 36$ at 350 K to $\langle n_{loop}\rangle \approx 30$ at 450 K. This is in contradistinction to our results for FRC and contrary to expectations based solely on the assumption of segment length-dependent (only) chemical potentials. This decrease in loop length is probably due to significant differences in torsional hindrances between loops and bridges or tails, arising from the introduction of preferred trans and gauche states in PE. Short loops require a higher proportion of gauche torsions and/or other high energy torsional states in order to fold back and reenter the crystal lamella, and thus are disfavored energetically relative to bridges or tails of comparable length. The relevant Boltzmann weight in this case, $\exp(-E_{tors}/kT)$, penalizes short loops at low temperatures, but this penalty decreases at higher temperatures. For this reason, the temperature dependence of the loop population for PE differs from both the bridge and tail populations as well as from the results for FRC. As an aside, the average length of loops is invariably smaller than that for bridges, because the width of the interlamellar phase imposes a minimum length for bridges, but not for loops.

Next, we consider the equilibrium topology of the {201} crystal/amorphous interface in polyethylene. The equilibrium topology in terms of length, orientation and ordering of bridges, loops and tails is important not only for material properties of the interlamellar phase, but also represents the end state for relaxation of the interface long after crystallization has stopped. Here, we focus on the loop statistics and introduce a notation in which $[mn0]$ describes the reentry vector or end-to-end vector for a loop segment, $[\pm ml_x, \pm nl_y, 0]$, with l_x and l_y representing the projected length of a unit cell vector (a or b) at the crystal surface in the x- and y-directions, respectively. In polyethylene, the difference in setting angles of the crystal stems at each end of a loop of type $[m/2\ n/2\ 0]$ allows us to differentiate between vectors of different length but a common crystallographic direction (e.g., $[{}^1/_2{}^1/_2 0]$ and [110]) by small changes in reentry angles. For all other crystallographic directions, where the setting angles of the crystal stems at both ends of the loop are the same, loops of different reentry vector length but common direction (e.g., [100] and [200]) are lumped together; in such cases, the loops with shortest contour length are always statistically the most important, so we make the simplifying assumption that each direction is dominated by loops with the shortest reentry vector. Figure 5 shows results for both FRC and PE at the same density and temperatures of 350 and 450K. It demonstrates the effects of torsional contribution and temperature on loop topology. The labeling order on the x-axis is chosen such that the shortest reentry vector length in a particular direction increases from left to right. Our first observation is that loops with reentry vectors oriented in the $[0n0]$ direction are the most common. This population is dominated by the [010] loops, which are the shortest of all possible loops in the {201} interface for the pseudohexagonal unit cell considered here. Second, the loop populations decrease from left to right, as the dominant loop reentry points become increasingly far apart. Last, the "*rest*" population is comprised exclusively of loops with reentry vectors longer than that for the [110] direction. The increase in this fraction of the loop population for PE relative to that in FRC is consistent with the shift toward longer loops in PE.

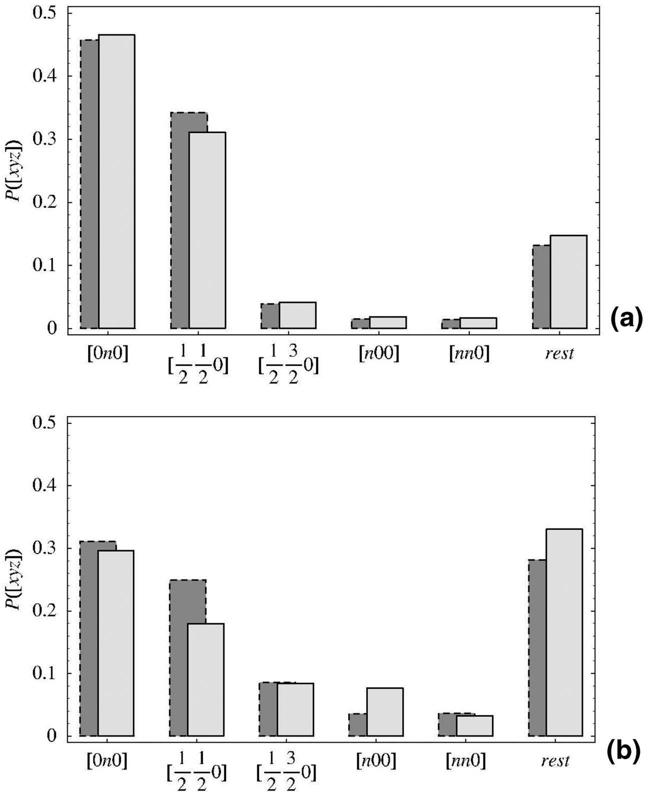

Figure 5. Reentry distribution at the undeformed state of (a) freely rotating chains, and (b) polyethylene as a function of reentry orientation at two temperatures: light bar, 350 K; dark bar, 450 K. The last entry "*rest*" lumps together all the remaining loops not explicitly considered in the other sets. The shortest reentry vector length in a particular direction increases from left to right. See text for notation.

The main factors contributing to the preferred loop reentry vectors are the minimum loop length required to traverse the distance, stiffness of the polymer backbone, and temperature. For both PE and FRC, the chemical potential advantage of short loops relative to long loops ensures that directions with short reentry vectors are most common; this is the most prevalent feature of the interlamellar phase topology. The backbone stiffness due to the bond angle bending and torsion potentials is the next most important factor in determining the reentry topology, shifting the distribution toward longer loops for PE more than for FRC. Reconstruction of reentry topology associated with changes in temperature between 350 and 450 K has a relatively small effect.

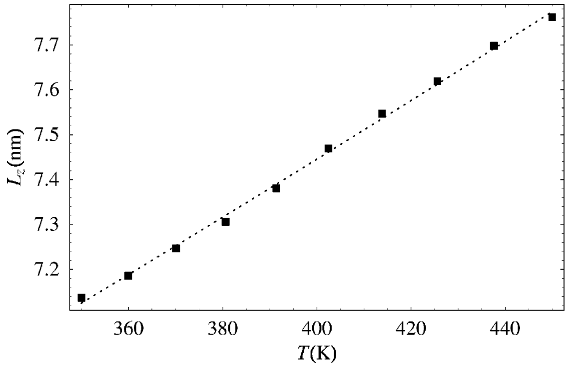

Figure 6. Interlamellar spacing at atmospheric pressure in the interlamellar phase.

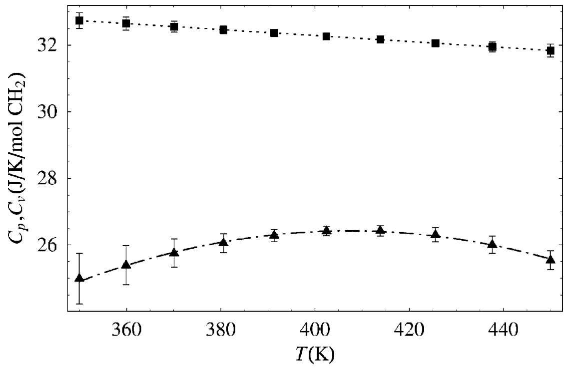

Figure 7. Heat capacities at atmospheric pressure: (■) C_p; (▲) C_v.

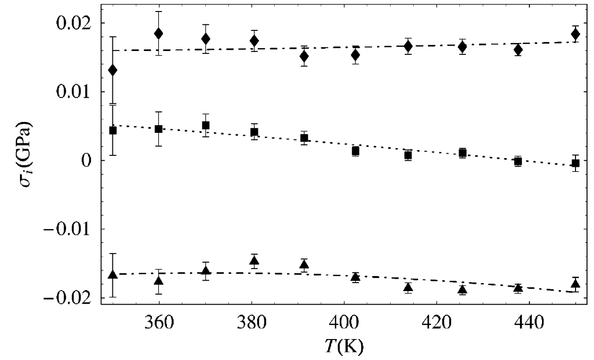

Figure 8. Diagonal components of the stress tensor at atmospheric pressure: (■) σ_1; (▲) σ_2; (◆) σ_3.

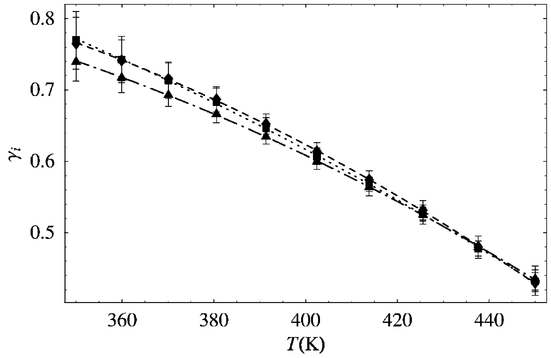

Figure 9. Grüneisen coefficients at atmospheric pressure: (■) γ_1; (▲) γ_2; (◆) γ_3.

Stresses and Thermal Properties. In the following discussion we make comparisons, where applicable, with experimental results for both semicrystalline and amorphous melt polyethylene at atmospheric pressure. In some instances, we have extrapolated the experimental data for semicrystalline or melt polyethylene to temperatures above or below, respectively, the melting temperature of 410 K. Such extrapolations are used only to provide upper and lower bounds by which to judge the validity of the simulated results. It is worth noting that, even though we are studying a component of a semicrystalline material, our results are expected to resemble the experimental melt results more closely than those of the full semicrsytalline material, since we are simulating and analyzing the noncrystalline interlamellar phase only.

First we discuss the structure and properties of the temperature-dependent reference volume systems (i.e., those at $P = 1$ atm). Figure 6 shows the thermally induced interlamellar distance needed to maintain atmospheric pressure in the interlamellar domain as the temperature is varied. From the slope of this line, the linear coefficient of thermal expansion of the interlamellar phase in the direction normal to the crystal surface is determined to be 8.3×10^{-4}/K, which compares favorably with an experimental value of 7.2×10^{-4}/K for a PE melt over the same temperature range.[27] The z-direction component behaves the most like bulk melt polyethylene, since the presence of crystalline lamellae does not constrain expansion in that direction.

Figure 7 displays the apparent isobaric and isochoric heat capacities as functions of temperature for the interlamellar domain at atmospheric pressure. We use the term “apparent” because the heat capacity of the interlamellar phase includes latent heat contributions due to shifts of the Gibbs dividing surface with temperature, as shown in Figure 4; this effect contributes to the temperature dependence of the apparent heat capacity and has been discussed in detail elsewhere.[16] For the interlamellar phase, $C_v(T)$ increases modestly with temperature up to 400 K, then decreases thereafter. The simulated isochoric heat capacity was also checked using the fluctuation formula,[28] with consistent results. The isobaric heat capacity $C_p(T)$ at $P = 1$ atm ranges from 32.8 to 31.7 J/K/mol CH$_2$ for temperatures from 350 to 450 K. This heat capacity corresponds to that of the entire interlamellar domain, including contributions from both amorphous and interfacial components. By comparison, extrapolated experimental values of an amorphous polyethylene melt at atmospheric pressure range from 33.1 to 37.8 J/K/mol CH$_2$ at the same pressure and temperatures.[29]

Figure 8 displays the diagonal components of the stress tensor as functions of temperature at atmospheric pressure. The z-component of stress is indicative of a system under tension in the direction normal to the lamellar surface, while the y-component indicates compression in the plane of the lamellar surface parallel to the b crystallographic axis. The x-component of stress is approximately zero over the whole range of temperature. This can be understood in terms of the reduction of the areal density of chains crossing the {201} surface relative to the {001} surface. In the b-axis direction, the distance between points where chains intersect the {201} surface is unchanged relative to the {001} surface; the compressive stress is indicative of congestion due to a competition between chain packing and conformational disordering. In the ac-plane (the x-direction), the tilt of chains relative to the surface increases the distance between points where chains intersect the {201} surface relative to the {001} surface. The degree of chain tilt corresponding to the {201} surface is just enough to eliminate any net tensile or compressive stresses in this direction.

Figure 9 reports Grüneisen parameters for the PE interlamellar phase as a function of temperature, which are lower than our previous results for FRC.[17] However, the system pressures computed in our previous work ranged from 0.13 to 0.25 GPa

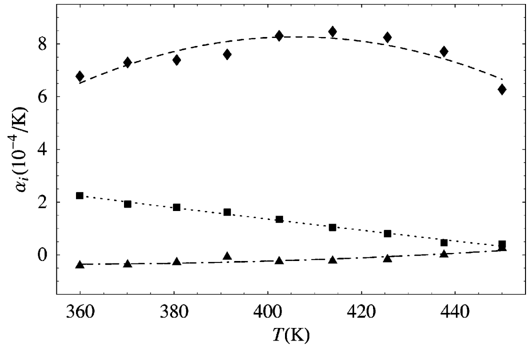

Figure 10. Thermal expansion coefficients as functions of temperature at atmospheric pressure: (■) α_1; (▲) α_2; (◆) α_3.

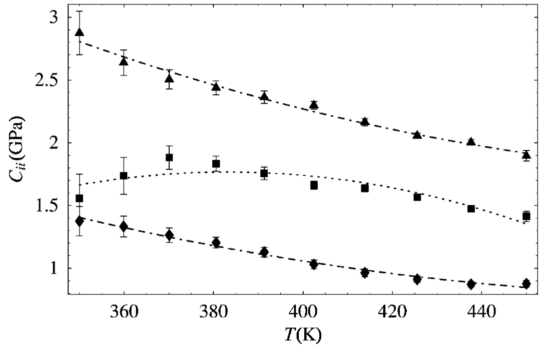

Figure 11. Diagonal tensile contributions to the elastic stiffness matrix at atmospheric pressure: (■) C_{11}; (▲) C_{22}; (◆) C_{33}.

(1300−2500 atm), significantly higher than the constant pressure of 1 atm studied here. Even though lower pressure would generally be expected to accompany an increase in configurational entropy, the introduction of the torsion potential in this case stiffens the chains and should serve to lower the conformational entropy. On the basis of these results, the stiffening effect of the torsion potential appears to be the dominant effect.

Figure 10 reports the coefficients of linear thermal expansion as functions of temperature. The coefficients were calculated as described in previous work,[17] assuming that $\gamma_5 \ll \gamma_{1,\,2,\text{ or }3}$, and interpolated to volumes corresponding to atmospheric pressure conditions. From these, the bulk thermal expansion coefficient is computed using $\alpha_{\text{bulk}} = {}^1\!/\!_3(\alpha_1 + \alpha_2 + \alpha_3)$. Comparison of the bulk thermal expansion coefficient with experimental melt values shows that simulated noncrystalline values range from 2.2×10^{-4}/K to 3.2×10^{-4}/K; these are about one-third to half of the experimental values for the amorphous melt, which range from 7.11×10^{-4}/K to 7.23×10^{-4}/K under comparable conditions.[27] The main difference between the interlamellar phase and the melt stems from the presence of the interfaces with the neighboring crystal lamellae in the interlamellar phase material. Continuity between the two phases results in lower coefficients of linear thermal expansion for the noncrystalline material in the plane of the interface, as shown in Figure 10, relative to those in the unconstrained melt. Values of α_3, the coefficient of linear thermal expansion in the direction perpendicular to the crystal surface, accord with values estimated earlier from Figure 5.

Elastic Properties. Figures 11 and 12 show the diagonal tensile components C_{ii}, where $i = 1, 2, 3$. (Voigt notation) and the off-diagonal tensile components C_{ij}, where $ij = 12, 13, 23$, respectively. At constant pressure, the stiffnesses decrease with increasing temperature, as expected.[30]

The shear components were calculated as functions of temperature, but only for deformation about a single reference cell, $\mathbf{h}_0$ ($T = 435$ K). Thus, we report the first estimate of the full stiffness tensor **C** for the noncrystalline interlamellar material in PE at $P = 1$ atm and at $T = 435$ K:

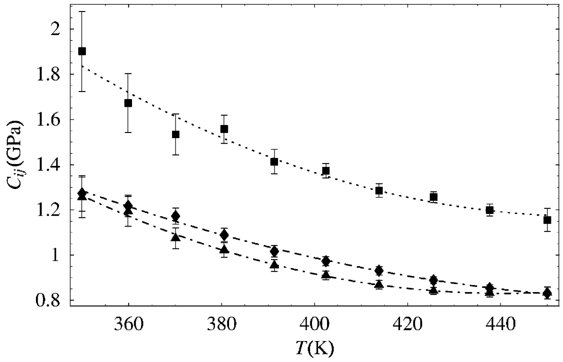

Figure 12. Off-diagonal tensile contributions to the elastic stiffness matrix at atmospheric pressure: (■) C_{12}; (▲) C_{13}; (◆) C_{23}.

$$\mathbf{C}(435\text{ K})\,[\text{GPa}] = \begin{pmatrix} 1.54 & 1.21 & 0.83 & 0.00 & -0.18 & 0.00 \\ 1.21 & 2.02 & 0.87 & 0.00 & -0.24 & 0.00 \\ 0.83 & 0.87 & 0.90 & 0.00 & 0.05 & 0.00 \\ 0.00 & 0.00 & 0.00 & \sim 0.00 & 0.00 & -0.20 \\ -0.18 & -0.24 & 0.05 & 0.00 & 0.22 & 0.00 \\ 0.00 & 0.00 & 0.00 & -0.20 & 0.00 & 0.57 \end{pmatrix} \quad (14)$$

The stiffness tensor exhibits monoclinic symmetry. This symmetry is due to the contribution of the interfacial component, which reflects in part the structure of the underlying crystal lamellae, and can be understood as follows. The unit cell of the crystal lamellae exhibits pseudohexagonal or orthorhombic symmetry. However, upon rotation of the crystal about the b-axis in order to orient the {201} surface in the plane normal to the z direction of the interlamellar domain, the stiffness tensor components take the general form $C'_{ijkl} = R_{im}R_{jn}C_{mnrs}R^T_{rk}R^T_{sl}$, with C_{mnrs} and C'_{ijkl} being components of the 4th order stiffness tensor before and after rotation, respectively, and the R_{ab}'s being components of the 3×3 rotation matrix; Einstein summation of repeated indices is assumed.[31] This results in the stiffness matrix for the crystal lamella exhibiting monoclinic symmetry in the frame of reference of the interlamellar domain. The interfacial contribution to elastic stiffness of the interlamellar phase also reflects this symmetry, through its structural connectivity to the crystal phase. The uncertainty in each of the tensile stiffnesses is ±0.03 GPa; the uncertainty in each of the shear stiffnesses is ±0.06 GPa, with the exception of C_{44}, where the uncertainty is closer to ±0.1 GPa. Within the accuracy of the shear deformation we employed, we were unable to determine a value for C_{44} significantly different from zero. As a result of this uncertainty, the determinant of the matrix in eq 14 is also zero, within the accuracy of the method, which indicates that the system is at best only marginally stable with respect to shear in the interlamellar phase.

The elastic compliance matrix is obtained by inversion of the stiffness matrix, $\mathbf{S} = \mathbf{C}^{-1}$, at $P = 1$ atm and $T = 435$ K. The uncertainty in C_{44} does not affect most of the compliances, but it does result in unreliable values for S_{44} and S_{66} by this process. To account for the effect of this uncertainty on the elastic compliances, we have instead generated numerically a large number ($O(10^4)$) of representative stiffness matrices by assuming random deviations δC_{ij} about the mean values of C_{ij} as dictated by the estimated uncertainty in each value, inverted each of these stiffness matrices, and then taken the average to obtain the best estimate of the compliance matrix $\mathbf{S} = \langle(\mathbf{C} + \delta\mathbf{C})^{-1}\rangle$:

$$\mathbf{S}(435\ \mathrm{K})\ [1/\mathrm{GPa}] = \begin{pmatrix} 2.0 & -0.34 & -1.6 & 0 & 1.6 & 0 \\ -0.34 & 1.3 & -1.0 & 0 & 1.3 & 0 \\ -1.6 & -1.0 & 3.7 & 0 & -3.2 & 0 \\ 0 & 0 & 0 & -6.0 & 0 & -2.3 \\ 1.6 & 1.3 & -3.2 & 0.0 & 8.3 & 0 \\ 0 & 0 & 0 & -2.3 & 0 & 0.85 \end{pmatrix} \quad (15)$$

From this, we estimate the Young’s moduli, $E_i = 1/S_{ii}$, $i = 1, 2, 3$, and the shear moduli, $G_{i-3} = 1/S_{ii}$, $i = 4, 5, 6$, and obtain the following values (in GPa) for the interlamellar phase of PE: $\{E_i, i = 1, 2, 3\} = \{0.49, 0.77, 0.27\}$; $\{G_i, i = 1, 2, 3\} = \{-0.17, 0.12, 1.17\}$. The bulk modulus of the simulated interlamellar phase, defined as $K = 1/((S_{11} + S_{22} + S_{33}) + 2(S_{12} + S_{13} + S_{23}))$,[32] is found to be 0.89 GPa. Reported experimental bulk moduli for a PE melt range from 1.38 to 0.87 GPa at 350 to 450 K, respectively, and from 3.37 to an extrapolated value of 0.84 GPa for semicrystalline PE at the same temperatures.[30] Stresses arising from deformation of the crystal lattice were excluded from the calculation, so the interlamellar material is expected to be stiffer than the pure melt, due to the influence of the interface regions, yet not as stiff as the experimental values for semicrystalline PE, which include crystal phase contributions. The values for Young’s moduli of the interlamellar phase are roughly in accord with values between 0.02 and 0.4 GPa estimated by Crist et al. using a two-phase composite model.[10] Because of the initial uncertainty in C_{44}, we feel that G_1 and G_3 should be interpreted with caution, but that the estimates for E’s, G_2, and K are all reliable. We can also say with some confidence that $G_1 < G_2 < G_3$, which can be rationalized as follows. G_3 represents in-plane shear of the interphase, which is most strongly resisted by short loops. G_2 represents shear across the axes of the chains, which are tilted in the *xz*-plane as they enter the interphase from the neighboring crystal phase. G_1 represents sliding of sheets of tilted chains relative to one another, which does not cut across chain axes and therefore is most compliant. Significantly, Krigas et al. reported a plateau shear modulus for the amorphous melt on the order of 0.002 GPa; this is below the limit of precision of our simulations and consistent with our difficulty in determining an accurate value of G_1.[33]

Conclusion

In this work, we report the results of atomistic Monte Carlo simulations for the thermoelastic properties of the semicrystalline interlamellar phase in polyethylene using a fully realistic model of polyethylene, complete with 3-fold torsional potential. We compare these with what we observed previously for the freely rotating chain model and with experimental data, where available. In studying both the density and order profiles, we find that the interphase thickness decreases with increasing temperature, in accord with previous results for FRC. However, the trend is weaker in PE than in FRC, which is attributed to the stiffening of PE chains due to the torsion potential.

Results from loop reentry distributions show that the preferred reentry vector on the {201} surface of PE is along [0*n*0], predominantly the [010] vector, followed by the [$^1/_2{}^1/_2$0] vector. This is switched from our previous results for FRC,[13] but the difference can be traced to the use of a different unit cell for PE in this work. Gautam et al. used the experimentally determined orthorhombic unit cell, whereas the current work uses the equilibrium pseudohexagonal unit cell at $P = 1$ atm, according to the united atom force field of Paul et al.[18] However, in both cases, the predominant reentry vectors occur where the shortest loops are found. Bond angle stiffness and, for PE, torsional stiffness also play secondary roles in determining loop lengths. From an investigation of the temperature dependence of the average lengths of loop, tail, and bridge segments in PE, it was found that the average length of both bridges and tails increase with increasing temperature, as was the case for FRC. This is attributed mainly to the segment chemical potentials, which increase with chain length, such that lower temperatures favor shorter segments. In contrast, the average length of loops decreases with increasing temperature, opposite to what was found for FRC. This is attributed to the torsional potential, which disfavors the gauche states required to form short loops; as a consequence, lower temperatures favor longer loops. In general, trends of this type may be expected with increasing conformational stiffness in crystallizable polymers.

Thermal expansion coefficients of the interlamellar material behave more or less as expected. The coefficient of linear thermal expansion perpendicular to the crystal surface is similar to that of the bulk amorphous melt, whereas the coefficients parallel to the crystal surface mimic those of the crystal phase. The interlamellar phase is found to be under tension in the direction perpendicular to the lamellae and in compression in the plane of the crystal surface and parallel to the *b*-direction of the unit cell (the *y*-direction of the simulation cell). The degree of chain tilt corresponding to the {201} surface is just enough to eliminate any compressive stresses in the *x*-direction.

Isothermal elastic stiffnesses are reported for the first time for a realistic molecular model of the PE interlamellar phase. Furthermore, both tensile and shear stiffnesses were determined, as well as the temperature dependence of tensile stiffnesses at $P = 1$ atm. From the full elastic stiffness matrix determined at 435 K, the elastic compliance matrix, Young’s moduli and shear moduli were determined. The bulk modulus was found to lie intermediate between the experimental values reported for a purely amorphous melt and the semicrystalline solid, providing good support for the quantitative accuracy of the PE interlamellar phase model and, a posteriori, for the conditions of metastability on which it is predicated. Estimates of the mechanical properties of the interlamellar phase from molecular modeling of this type, in conjunction with similar estimates for the mechanical properties of the crystal phase[34] should prove invaluable as parameters for input to composite models of semicrystalline polymers with different morphologies that may arise as a result of processing history, for example.

Acknowledgment. This work has been supported by the Center for Advanced Engineering Fibers and Films through the ERC program of the National Science Foundation under Award ECC-9731680, by the MRSEC Program of the National Science Foundation under Award DMR-9808941 and by the Swiss National Science Foundation under Grant 81EZ-68591.

References and Notes

(1) Strobl, G. R.; Hagedorn, W. *J. Polym. Sci. B* **1978**, *16*, 1181.
(2) Naylor, C. C.; Meier, R. J.; Kip, B. J.; Williams, K. P. J.; Mason, S. M.; Conroy, N.; Gerrard, D. L. *Macromolecules* **1995**, *28*, 2969.
(3) Olley, R. H.; Hodge, A. M.; Bassett, D. C. *J. Polym. Sci.* **1979**, *17*, 627.
(4) Boyd, R. H. *Polymer* **1985**, *26*, 1123.
(5) Kerner, E. H. *Proc. Phys. Soc. London* **1956**, *69B*, 808.
(6) Uemura, S.; Takayanagi, M. *J. Appl. Polym. Sci.* **1966**, *10*, 113.
(7) Christensen, R. M. *J. Mech. Phys. Solids* **1990**, *38*, 379.

(8) Christensen, R. M.; Lo, K. H. *J. Mech. Phys. Solids* **1979**, *27*, 315.
(9) Gardner, S. D.; Pittman, C. U., Jr.; Hackett, R. M. *Compos. Sci. Technol.* **1993**, *46*, 307.
(10) Crist, B.; Fisher, C. J.; Howard, P. R. *Macromolecules* **1989**, *22*, 1709.
(11) Balijepalli, S.; Rutledge, G. C. *J. Chem. Phys.* **1998**, *109*, 6523.
(12) Balijepalli, S.; Rutledge, G. C. *Comput. Theor. Polym. Sci.* **2000**, *10*, 103.
(13) Gautam, S.; Balijepalli, S.; Rutledge, G. C. *Macromolecules* **2000**, *33*, 9136.
(14) Rutledge, G. C. *Macromol. Sci. Phys.* **2002**, *B41*, 909.
(15) Debenedetti, P. G. *Metastable Liquids: Concepts and Principles*; Princeton University Press: Princeton, NJ, 1996.
(16) Hütter, M.; In ‘t Veld, P. J.; Rutledge, G. C. *Polymer*, **2005**, in press.
(17) In ‘t Veld, P. J.; Rutledge, G. C. *Macromolecules* **2003**, *36*, 7358.
(18) Paul, W.; Yoon, D. Y.; Smith, G. D. *J. Chem. Phys.* **1995**, *103*, 1702.
(19) Bolton, K.; Bosio, S. B. M.; Hase, W. L.; Schneider, W. F.; Hass, K. C. *J. Chem. Phys. B* **1999**, *103*, 3885.
(20) Waheed, N.; Lavine, M. S.; Rutledge, G. C. *J. Chem. Phys.* **2002**, *116*, 2301.
(21) Ko, M. J.; Waheed, N.; Lavine, M. S.; Rutledge, G. C. *J. Chem. Phys.* **2004**, *121*, 2823.
(22) Theodorou, D. N.; Boone, T. D.; Dodd, L. R.; Mansfield, K. F. *Makromol. Chem. Theory Simul.* **1993**, *2*, 191.
(23) Bassett, D. C.; Hodge, A. M. *Proc. R. Soc. London A* **1981**, *377* (1768), 25.
(24) Hoffman, J. D.; Miller, R. L. *Polymer* **1997**, *38*, 3151.
(25) Kofke, D. A. *J. Chem. Phys.* **2002**, *117*, 6911.
(26) Parrinello, M.; Rahman, A. *J. Appl. Phys.* **1981**, *52*, 7182.
(27) Orwoll, R. A.; Flory, P. J. *J. Am. Chem. Soc.* **1967**, *89*, 6814.
(28) Allen, M. P.; Tildesley, D. J. *Computer Simulation of Liquids*; Clarendon Press: Oxford, U.K., 1986; Chapter 2.
(29) Gaur, U.; Wunderlich, B. *J. Chem. Phys. Ref. Data* **1981**, *10*, 119.
(30) Olabisi, O.; Simha, R. *Macromolecules* **1975**, *8*, 206.
(31) Rutledge, G. C.; Suter, U. W. *Polymer* **1991**, *32*, 2179.
(32) Nye, J. F. *Physical Properties of Crystals.* Oxford University Press: Oxford, U.K., 1985.
(33) Krigas, T.; Carella, J. M.; Struglinski, M. J.; Crist, B.; Greassley, W. W.; Shilling, F. C. *J. Polym. Sci., Polym. Phys. Ed.* **1985**, *23*, 509.
(34) Rutledge, G. C. Modeling Polymer Crystals. In *Simulation Methods for Polymers*; Kotelyanskii, M., Theodorou, D. N., Eds.; Marcel Dekker: New York, 2000; Chapter 9.

MA0518961